(article starts on next page)

Contents lists available at ScienceDirect

Journal of Catalysis

journal homepage: www.elsevier.com/locate/jcat

The role of polaronic states in the enhancement of CO oxidation by single-atom Pt/CeO$_2$

Minttu M. Kauppinen [a,b,1], Nathan Daelman [c,1], Núria López [c], Karoliina Honkala [a]

[a] *Department of Chemistry, Nanoscience Center, University of Jyväskylä, P.O. Box 35, FI-40014 Jyväskylä, Finland*
[b] *Department of Physics and Competence centre for Catalysis, Chalmers University of Technology, SE-412 96 Göteborg, Sweden*
[c] *Institute of Chemical Research of Catalonia (ICIQ), The Barcelona Institute of Science and Technology (BIST), Av. Països Catalans 16, 43007 Tarragona, Spain*

ABSTRACT

Single Atom Catalysts (SACs) have shown that the miniaturization of the active site implies new phenomena like dynamic charge transfer between isolated metal atoms and the oxide. To obtain direct proof of this character is challenging, as many experimental techniques provide averaged properties or have limitations with poorly conductive materials, leaving kinetic measurements from catalytic testing as the only reliable reference. Here we present an integrated Density Functional Theory-Microkinetic model including ground and metastable states to address the reactivity of Pt$_1$/CeO$_2$ for CO oxidation. Our results agree with experimentally available kinetic data in the literature and show that CO oxidation activity of Pt$_1$/CeO$_2$ is tunable via the electronic properties of the support. Particularly, samples with higher n-doping via oxygen depletion should be better in CO oxidation, as they help maintain the active state Pt^0 of the catalyst. This provides an alternative strategy for tuning the performance of low-temperature oxidations in single-atom catalysts via charge transfer control.

© 2023 The Author(s). Published by Elsevier Inc. This is an open access article under the CC BY license (http://creativecommons.org/licenses/by/4.0/).

1. Introduction

Single Atom Catalysts (SACs) have emerged as a new class of materials that bridges heterogeneous and homogeneous catalysis, benefiting from the properties of both [1,2]. The strategy of increasing noble metal dispersion lead to the isolated atom limit, [3] and the term *single-atom* was first coined when investigating CO oxidation activity of individually deposited Pt atoms on reducible iron oxide, FeO$_x$[4]. In the years following, the number of SAC applications has tremendously increased [5,1,6,7]. The miniaturization of the active sites comes with a strong electronic coupling between the metal atom and the host material. [8] Thus, the electronic states of the metal are better represented as an electronic ensemble, formed by the ground and few metastable states,[9] with metals in different oxidation states [10] following a similar rational to the geometric ensembles identified for small clusters [11] thus with the potential of breaking the well-established linear-scaling relationships.[12] The electron–phonon coupling has multiple effects in the properties of oxides [8] but their impact in reactivity of SACs are not fully understood.

Platinum dispersions supported by CeO$_2$ are particularly well-studied case due to their role in the three-way automotive exhaust post-processing [13–19], which covers the full combustion of CO and hydrocarbon and elimination of NO$_x$. Single-atom sites are among the dispersion types being investigated as novel candidates for clean, low-temperature oxidation catalysis [20,21]. Initially, these materials were thought to be constituted by rather small active nanoparticles (diameter< 1.4 nm) [15,16,22]. Several studies, however, report outstanding reactivity while preserving the dispersion [23,17,24,18] of low-nuclearity species that are reactive enough under realistic conditions to serve as catalytic centers. Still, there remains an ongoing debate over the exact nature of the active sites, since reactivities vary widely not just by size, but also preparation method (see Fig. 5c, Ref. [20]).

Meanwhile, there is wider agreement that the dormant catalyst has to be activated. Kinetic experiments show that light-off CO oxidation over as-prepared Pt$_1$/CeO$_2$ reaches full conversion at 250°C [25]. An activation step with reductive CO pulses boosts its reactivity further [25,16] lowering the full conversion temperature to 175°C [26] and the apparent activation barrier between 0.3 and 0.4 eV [16]. The extent of this activity enhancement varies with reductant gas (hydrogen [27], steam [21,18]) and temperature, but remains significant throughout. Reduction

---

[1] These authors equally contributed to this work.

of the support has been tied to vacancy formation, which can either directly participate in the reaction [21,28], or alter the coordination of the catalyst [27]. Excessive reduction or heating during synthesis [18] and pretreatments favor aggregation, though based on the high formation energy of Pt dimers, as computed by DFT [9], suggests that Ostwald ripening is more likely to occur than nucleation. As such, there is indication that single atoms can coexist with larger nanoclusters [19]. XPS and IR measurements have confirmed SA Pt on ceria synthesized via oxidative treatments to be ionic (2+) [13,29]. STM meanwhile, assigns the anchoring sites to stepped or nanostructured CeO_2 surfaces [13,29], with DFT indicating a local geometry that heavily favors fourfold coordination at exposed 100 terminations [29]. Such coordinations match up well with known Pt chemistry [30]. Tracking the state of SAs at operando conditions, however, faces the limitations of atomic-resolution microscopy and spectroscopy techniques [31,32]. This leaves experimental kinetics, i.e. the conversion rates and activation energies, as the most reliable benchmark for comparing simulations, once the nuclearity of the clusters has been characterized. Indeed, the best suggestions for the active state thus far come from EXAFS [33] or theory [34], coupled to kinetic results and point in the direction of the fourfold coordination distorting [33] or even breaking [34].

DFT has been used to suggest several varieties of the Mars-van Krevelen mechanism with CO adsorbing at Pt^{2+} and reacting with lattice oxygen. Typically, the vacancy healing proceeds via activated dioxygen, though steam [28] or labile oxygen formed at the step edges [34] have been shown to be more favorable. Lu et al. further expand on MvK, by suggesting two routes that either convert one or two CO adsorbates [34]. More recently, a monolayer Pt oxide film has been suggested as an alternative [18]. Some groups have explored a catalyst setup of coexisting oxidation state, consisting of Pt^{2+}, Pt^{4+}, and $Pt^{\delta+}$, that varies with temperature [19]. To the knowledge of the authors, there has been no attempt to build microkinetic models for any of these models.

To directly map the CO oxidation kinetic behaviour onto experiments, we employ microkinetic modelling (MKM) [35,36] based on the computed DFT reaction network and coupled to the external control variables, i.e. temperature and pressure, to obtain the time-evolution of the surface intermediates [37,38]. This approach is valid at low loadings, where the SAC can be thought of as isolated sites, thus equivalent to Kinetic Monte Carlo [39]. MKM is also a powerful analytics tool for retrieving the relevant catalytic domains [40], rate-determining steps, and surface coverages [38]. Furthermore, it enables descriptor-aided design [41,42], allows extensions towards high-pressure regimes [43] and can identify novel on-surface pathways [44]. Still, microkinetics are applied to the ground-state energy profile with singular, unique well-defined intermediates along the reaction coordinate [45]. While an extension to geometric ensembles has recently been considered for clusters [46], any such analysis for electronic ensembles is lacking. While outside the scope of the current work, it would be very desirable to evaluate the joint impact of both ensembles types on CO oxidation. Low-nuclearity Pt clusters namely show a remarkable adaptability or "fluxionality" with improved performance of O–H dissociation [47].

In this work, we present a microkinetic model for CO oxidation by SA $Pt/CeO_2(100)$, built from just DFT data. It is the first such model to also account for the dynamic change of the oxidation state of the Pt centre, which we handle as an electronic manifold in the MKM simulations. We show that inclusion of the electronic ensemble is necessary for achieving good agreement with experimental kinetics and deducing new catalytic design concepts.

2. Computational details

2.1. Density functional theory details

All energies and frequencies were computed using the Perdew-Buke-Ernzerhof (PBE) functional [48,49] as implemented in the Vienna Ab initio Simulation Package (VASP; version 5.4.4) [50–53]. Since regular GGA fails to capture the Density of States (DOS) in reduced rare-earth oxides [54], we employed a Hubbard correction with an effective on-site Coulomb interaction ($U_{eff} = 4.5$ eV) to the Ce 4f-orbitals [9,55]. While d-band materials similarly suffer from erroneous self-energy, no issues have been raised regarding the efficacy of GGA for platinum dioxide (PtO_2, α and β phase) [56,57]. Likewise, we retrieved the pre-conditions for oxidation state dynamics from with hybrid functionals (see Ref. [9], SI Fig. 9 and SI Table 3). Moreover, the introduction of Hubbard correction can lead in and of itself to biases in the thermodynamics and kinetics of charge transfer processes [58]. Considering the cost-benefit analysis, we thus prefer to keep the usage of Hubbard corrections to a minimum. The valence-electrons were modelled using a plane-wave basis set with a cutoff energy of 500 eV, while projector-augmented waves (PAW) describe the core-electrons including scalar-relativistic effects [59].

CeO_2 has a fluorite structure with an experimental lattice parameter of 5.410 Å. Nine-atom thick slab models consisting of a (3×3) supercell cleaved along the (100) direction were used, where the lower four layers were fixed to their bulk positions. A vacuum height of 15 Å was chosen to allow enough space for adsorbates to adsorb. This results in unit cell dimensions of 11.649 Å $\times$ 11.649 Å $\times$ 25.983 Å. The Brillouin zone was sampled using a gamma-centered, (3×3) k-mesh. To mitigate the inherent dipole moment of cleavage along the (100), half of the oxygen monolayer was moved to the bottom layer, analogous to Ref. [60]. Any further spurious dipole moment stemming from asymmetric adsorption was corrected using in the internal VASP routines [61,62] along the z-axis. To simulate the spontaneous reconstruction of the surface after cleavage, half of the top surface oxygen atoms were moved to the bottom layer. The remaining surface atoms are aligned according to most stable termination, with parallel rows of oxygen atoms alternating with trenches of vacancy sites. This provides the single-atom metal with two ligands. The single-atom itself was modelled as in Ref. [9], where a Pt adatom is located within the O-trenches, coordinating with two lattice oxygen atoms.

Transition states between different intermediates were obtained using climbing image NEBs[63] and verified by the harmonic frequency analysis. Various intermediates were found to possess higher energy metastable states, where some cerium ions are reduced by electrons originating from Pt. For the polarons, we approximated the hopping barrier similarly to Ref. [64], i.e. by comparing the energy difference between the states with a delocalized and localized electron. As such, we retrieve a polaron barrier of 0.37 eV for the jump from the neutral state to the most stable lattice site, closely matching the lattice hopping parameter found in Ref. [65]. Our barrier lies within the same range of polaron hopping barriers observed on the (111) surface ($0.23 - 0.50$ eV) [66,67]. The sensitivity of the microkinetic model with respect to the polaron hopping barriers was tested by increasing each hopping barrier one at a time by 0.2 eV and observing the response in the results. It was found that changing the barriers by 0.2 eV had no effect on TOFs, coverages, or cycle selectivities. This is consistent with the finding that the hopping steps do not have rate controlling character. Thus, we use the same estimate for polaron hopping barrier throughout the entire reaction model. A more conceptual overview on polarons is given in section SI 1.2. Lastly, the

energies of the gas-phase species were corrected in order to improve the thermodynamic description of the CO oxidation reaction, see section SI 1.3.

2.2. Microkinetic model

The set of elementary reactions included in the mean-field microkinetic (MFMK) model is represented diagrammatically in Fig. 1. For a list of elementary reactions and their labels, please refer to Table S3. The rate constants were calculated via the harmonic transition state theory using ZPE and entropy corrected activation free energies obtained from DFT calculations detailed in the previous section. To ensure thermodynamic consistency, the backward rate constants were calculated by dividing the forward rate constant by the equilibrium constant for each given elementary step. Furthermore, the total energies obtained from DFT for the gas-phase molecules were corrected in order to achieve a more accurate value for the total reaction energy (please see section SI 3 for numerical values and details). The entropies of the surface species were calculated in the harmonic limit as implemented in the HarmonicThermo class of the ASE Thermochemistry package, while the entropies for the gas-phase species were calculated in the ideal-gas limit using the IdealGasThermo class of the ASE Thermochemistry package.[68,69].

The Pt/CeO$_2$ active sites can be assumed to be very isolated from each other, as the Pt atom is reasonably firmly anchored to its ideal location on the CeO$_2$ support. The adsorbate–adsorbate interactions are included explicitly in the underlying DFT calculations. Thus, in our case the mean-field microkinetic model and a fully spatially resolved Kinetic Monte Carlo (KMC) model will yield equivalent results[39,70] removing the typical limitation, i.e. lack of lateral interaction effects, for MFMK models.

The system of differential equations was solved using our own Python-based script. The integration was carried out numerically with the solve_ivp function implemented in the Scipy package [71] scipy.integrate. The simulations were carried out at steady reaction conditions (i.e. constant temperature and pressure) for different gas-phase compositions mimicking lean and very lean conditions. Each simulation was carried out for a long enough time (10^5 seconds in general) to ensure that the steady-state was reached before the end of the simulation. To test the influence of the polaron hopping steps, additional simulations were performed with polaron hopping steps switched off (see SI for details). The apparent activation energy was determined from an Arrhenius plot (Fig. 4) generated for a 13:19 CO to O$_2$ ratio in the temperature range from 130 to 290° C. The conditions were chosen to match the experimental set up in previous experiments [26]. For additional detail, please refer to section SI 2.

3. Results

The reaction network for the 2 CO + O$_2$ → 2 CO$_2$ is shown in Fig. 1 and the corresponding PBE + U energy profile is given in Fig. S1. In this study, we offer an extended view on the CO oxidation reaction mechanism, building on the initial and more confined perspective presented in Ref. [9]. The full reaction network takes into account activation and deactivation routes, the reactivity in the electronic ensemble, and the extent of SA coordination, in particular the vital role a secondary carbonyl ligand plays in facilitating this ostensibly simple reaction. The name convention of species used throughout the work is explained in Section SI1.3 and listed in Table S1. The reaction consists of two partially overlapping cycles: the shorter Cycle I revolves around the twofold oxygen-coordination of the catalyst decorated by carbon-rich ligands, while the more oxygen-rich Cycle II switches coordination

between twofold, linear (2-s-oxo-Pt, II.1) and fourfold, square-planar (4-s-oxo-Pt, II.8) geometries. The appearance of multiple cycles stems from a changing coordination sphere under external reduction, similar to what was observed in Ref. [34], where the SAC lies at a step edge with {100} orientation. The system under consideration here is an extension of that surface, where the three-fold coordination is unstable and converts to a twofold one [9].

Surface species, such as 2-s-oxo-Pt (II.1) or carbonyl-2-s-oxo-Pt (A.4), exchange electrons with the lattice and thus exhibit multiple SA metal oxidation states (mOS) corresponding to separate potential energy surfaces (PES) for the CO oxidation reaction. The change in mOS can happen either by polaron hopping (with an energy barrier) or be chemically induced by adsorption of ligands (likely involving entropic barriers), see Methods and Sections SI 1.1 and SI 1.2. These fluctuations can then yield more exotic, short-lived oxidation states, such as Pt$_1^0$, which on longer time scales is indicative of bulk platinum. These charge transfer processes can be accurately traced in *ab initio* [9]. *The reaction network shows that with increasing ligands coverage on Pt, the PES tends to converge to a single electronic state corresponding to higher metal charge.*

Both cycles share a CO oxidation step (the carboxyl-mediated path) and diverge at the integration of an external oxygen source into carbonyl-2-s-oxo-Pt (A.4). In Cycle I, molecular O$_2$ adsorbs as a surface peroxo (O$_2^{2-}$), which gains two electrons by oxidizing the vicinal metal centre to Pt^{2+}. The SA stays in this oxidation state throughout most of Cycle I. Neither lattice O, nor Ce^{4+} are favorable adsorption sites, but integration into the trench (along with the reduction to peroxo) is exothermic by 0.55 eV. This feature is unique to row-terminated CeO$_2$ (100).[72] The surface peroxo, when anchored into the lattice, introduces local strain (Fig. S2). It is, however, also uniquely placed to act as a peroxo ligand for the SA. Its predisposition hereto is supported by the drastic increases in dispersion levels and sintering resistivity at significant peroxo coverages [73]. Alternatively, interaction with gas-phase CO and the formation of geminal dicarbonyl, as typically seen with SA Rh [74,18], leads to structural degradation of the platinum site. This route is also less relevant under oxidizing conditions. Due to its mOS and four ligands, the I.1 complex is attempting to enforce a square-planar geometry, and we observe a considerably wide $C - \widehat{Pt} - O$ angle (117°) that hampers the reaction of the carbonyl with the peroxo. This in turn leaves the metal centre open to a nucleophilic attack of the second gas-phase CO, which forms a more advantageous 53° angle with the peroxo species in I.2. Since peroxo is already activated, the O-O bond breaks upon the formation of a PtOC-OO activated complex (TS$_{I.3}$) and leads to immediate CO$_2$ desorption with an activation barrier of ($E_a = 0.21$ eV). The strain induced by the peroxo has disappeared in I.4 (Fig. S2), and as the lattice returns to equilibrium, it pushes the remaining oxygen ion (O^{2-}) towards Pt (A.1).

The newly formed structure A.1 is analogous to I.1, but with an oxygen ion instead of peroxo, and the CO capture and conversion proceed similarly along the *carboxyl-mediated path*. To compensate for the wide angle (161°) in A.1, another carbonyl group is added, leading immediately to the formation of a carboxyl-2-s-oxo-Pt intermediate (A.2), which is a clear structural precursor of CO$_2$. Thus, the activation barrier of 0.33 eV corresponds to Pt-C bond breaking (TS$_{A.3}$), which completes the full Cycle I. Note that in addition to the twofold coordination with the support, Pt always has a carbonyl ligand present, which acts as a protective group against direct oxidation during Cycle I.

Cycle II starts with the removal of the protective carbonyl-group to obtain the 2-s-oxo-Pt (II.1) structure. The dynamic oxidation state, where several low-lying oxidation states change as a function of time, as verified by Born–Oppenheimer Molecular Dynamics [9], is most pronounced here due to quasi-degeneracy
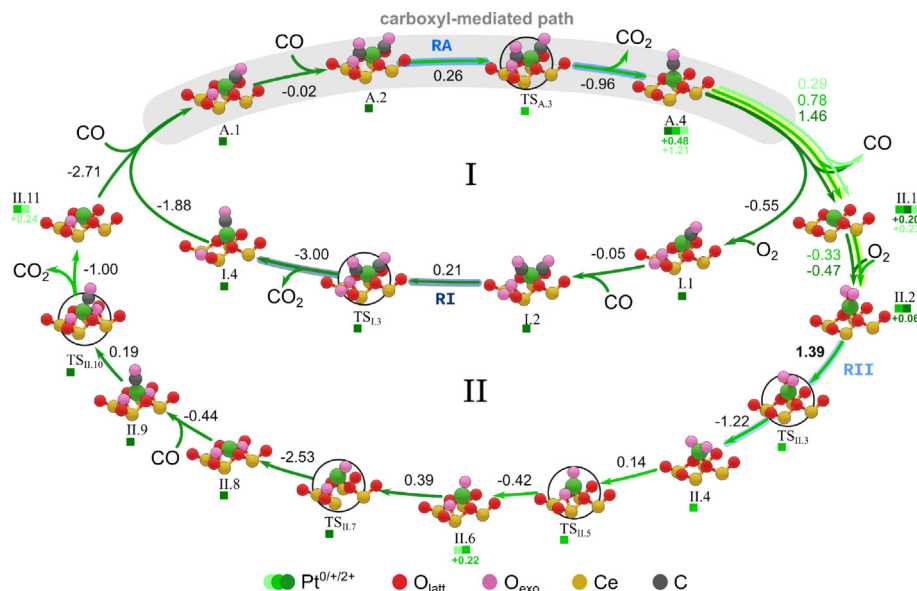
Fig. 1. Reaction network for CO oxidation over single-atom Pt_1/CeO_2 with the relative energy at each step. Depending on the atmospheric composition, the reaction progresses along one of two cycles (I: carbon-rich/II: oxygen-rich) that converge at the carboxyl-mediated path (grey shade). The intermediates and transition states (circled) local geometry -the metal complex and top surface layer- with their index and the Pt oxidation states as a footer (atomic colour code at the bottom). Oxidation states are ordered from left to right according to increasing electron transfer energy, referenced with respect to the ground state. Reactions with multiple PES follow the same conventions, and those with inhibited polaron hopping are highlighted in yellow. The rate-determining steps for each cycle, as determined by microkinetics (see below), are highlighted in shades of blue, see text. (For interpretation of the references to colour in this figure legend, the reader is referred to the web version of this article.)

(energy span of 0.30 eV). Molecular O_2 has now space to chemisorb onto the unprotected metal centre and oxidize it to bidentate η_2-dioxo-2-s-oxo-Pt (II.2), with the Pt oxidation state being either 1 + or 2+. The newly added ligands only bind to the metal but not the oxide surface, thus significantly weakening the bond between the metal and its support to the point where Pt is lifted out of the surface plane by $0.92 - 1.01$ Å. In the next step, the O-O bond breaks ($TS_{II.3}$) with an activation barrier of $E_a = 1.39$ eV, the highest barrier in both cycles. The bond breaking forces the system into a single oxidation state, bis(oxo)-2-s-oxo-Pt^+ (II.4). For more information on both intermediates, see Section SI 1.4. The under-coordinated oxygen ligands in the II.4 intermediate integrate one-by-one into the (100) trench orthogonal to $PtO_{2,upper}$ (Fig. S3). In the following steps, the II.4 intermediate reacts to form oxo-3-s-oxo-$Pt^{0/+}$ (II.6) with $E_a = 0.14$ eV, and subsequently 4-s-oxo-Pt^{2+} (II.8), with $E_a = 0.40$ eV and an overall exothermicity of 2.40 eV. This intermediate (4-s-oxo-Pt^{2+}) will not convert back to 2-s-oxo-Pt and surface oxygen (endothermic by 2.31 eV), being the most stable Pt-O combination.

In the coordination chemistry of platinum, the 2+ oxidation state is known to favor fourfold coordination [30]. Likewise, its heterogeneous counterparts exhibit strong adsorption energies, as reported in Ref. [9] or demonstrated here with intermediate II.8. Note that the main difference between both cases is the oxygen stoichiometry. Since surface diffusion of oxygen only becomes relevant at temperatures of 800 K or above [75], and because O_2 partial pressures as low as 5×10^{-2} mbar block on-surface transport of oxygen [76], we exclude the formation 4-s-oxo-Pt^{2+} via surface restructuration alone.

Finally, to reactivate the square-planar resting state, II.8, CO first adsorbs onto the metal centre, forming the carbonyl-4-s-oxo-Pt^{2+} (II.9) species. Due to its orthogonal orientation to the square-planar ring, the carbonyl-ligand has a vantage point to attack one of the oxygen ligands ($TS_{II.10}$) and the resulting E_a is only 0.19 eV. CO_2 desorption breaks up the coordination shell producing a carbonyl-3-s-oxo-Pt (II.11) intermediate, with Pt once again having two possible oxidation states 0 and 1+. At this point, Cycles I

and II converge as the catalyst proceeds to the next round of CO conversion.

This concludes the DFT analysis of Cycle I and Cycle II, which mainly differ in how they bind gas-phase oxygen, either near or at the metal site, leading to peroxo/superoxo which in turn affects the O-O bond activation. Subsequent CO oxidation steps proceed similarly in both cycles, and the DFT results suggest that Cycle II will contribute less to the conversion rates than Cycle I, due to the high O-O bond breaking barrier ($TS_{II.3}$). We therefore propose that the twofold/ fourfold coordinations correspond to the experimentally observed active/resting state of the catalyst [13,29].

The next step is to connect the reaction network to the experimental kinetic studies. Experiments have been conducted at a wide range of temperatures, pressure, and flow rates, and based on the detailed analysis we will concentrate on the results in Ref. [[26]]. To mimic the experimental conditions, we chose to simulate the reaction at atmospheric pressure with CO to O_2 ratios of $1:1$ and $1:9$, with 1e-5 bar CO_2. Simulations were carried out at temperatures ranging from 25 to 225°C at 10°C intervals. Note that the fractional coverage of a species is the fraction of SA occupied across the population of all SA sites.

We performed a set of kinetic analyses for each gas-phase composition to assess the behaviour of the system. In order to determine which reaction steps are rate controlling, the degree of rate control, X_{rc}, was calculated for each elementary step in the reaction network. Three reactions (RI, RII, and RA, presented in Fig. 2) were found to have significant X_{rc} values (see Fig. 3), and thus control the overall CO_2 production rate throughout the whole temperature range considered. As the reactions RI and RII correspond to Cycle I and II, respectively, and RA is common to both cycle, the TOFs and X_{rc} values of RI and RII can be used to determine which cycle dominates at any given reaction condition.

At low temperature for both gas compositions, reaction RI is the most rate controlling, with an X_{rc} value of circa 0.65, while RA has an X_{rc} value of 0.35. This indicates that Cycle I is dominating at low temperatures, which is confirmed by a selectivity S_I value of one. As the temperature increases, the rate controlling character of RII
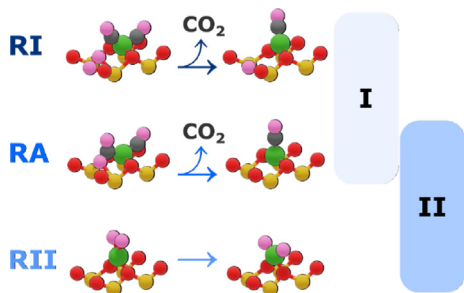
Fig. 2. Key steps RA, RI, and RII with significant rate control in the total reaction mechanism. The steps are also labeled in the cycle representation in Fig. .1.

increases further and goes through a maximum (c.a. 155° C for the 1 : 1 composition and c.a. 105° C for 1 : 9 see Fig. 3) before falling off at elevated temperatures. The X_{rc} value of RII starts to increase when the X_{rc} of RI has reached its maximum. The X_{rc} of RA initially decreases with increasing temperature, but starts to rapidly increase again at around 195° C for composition 1 : 1, whereas for the 1 : 9 composition the increase in X_{rc} starts already at 125° C. As Fig. 3 demonstrates, the fractional coverages of species I.1 and A.1, correlate extremely closely with the rate controlling character of RI and RA, respectively, because they are the reactant species of the steps immediately preceding them. For the composition 1 : 9, a slight offset is seen for the correlation between I.1 coverage and RI, whereas for composition 1 : 1 the correlation stays better. The correlation between X_{rc} and coverage remains throughout the whole temperature range for RA and A.1, and does not depend on gas ratio.

The selectivity S_I towards Cycle I or S_{II} towards Cycle II are defined as $S_X = r_X/(r_I + r_{II})$ where 'X' stands for either I or II, and r_I/r_{II} is the rate of RI/RII. The resulting plot of selectivities is presented in Fig. 3. The selectivity switch-over from Cycle I to Cycle II starts to occur concurrently with the fall/rise of the rate control

of RI/RII. When $S_I = S_{II} = 0.5$, the rate control is also equally shared between RI and RII. This occurs at a much lower temperature for the 1 : 9 gas ratio. The switch-over from Cycle I to Cycle II is complete after RII has reached maximum rate control. At high temperatures the rate determining step (RII or RA) depends on the gas-composition, but there is no effect on the cycle selectivity when the rate control switches from RII to RA. The switch-over from Cycle I to Cycle II with rising temperature can be explained in terms of the stability of the CO ligand. Cycle I requires the presence of at least one CO ligand at all times for the reaction to proceed, but as the temperature increases (or CO partial pressure is lowered), desorption from the site becomes more favourable. The removal of the CO ligand forces the reaction to proceed through Cycle II.

A low temperature for both gas compositions the reaction order with respect to CO starts at a constant value of 1, but rapidly starts to fall off towards zero at elevated temperatures. The curve perfectly traces the falling selectivity towards Cycle I. For the 1 : 9 gas-composition, the CO reaction order reaches a minimum at 155° C, then rapidly rising again and following the curve of the RA X_{rc} value. The positive reaction order of CO is rationalized as the RI and RA reactions proceed through intermediates with two CO molecules bound to the SA, therefore higher CO partial pressures will drive the reaction forward.

The reaction order with respect to oxygen is zero at low temperature for both compositions, as Cycle I is not as sensitive to the oxygen pressure. For the lean composition, the reaction order rises following the Cycle II selectivity curve. The correlation is due to the most abundant surface species being the ligand free II.1 species. For the 1 : 9 composition, the reaction order rises with temperature only slightly from zero. This is due to the rate controlling step being RA, which is not sensitive to oxygen pressure.

4. Discussion

To directly relate our results to experiments, we have computed the light-off temperature curves, Fig. 4, comparing the turnover
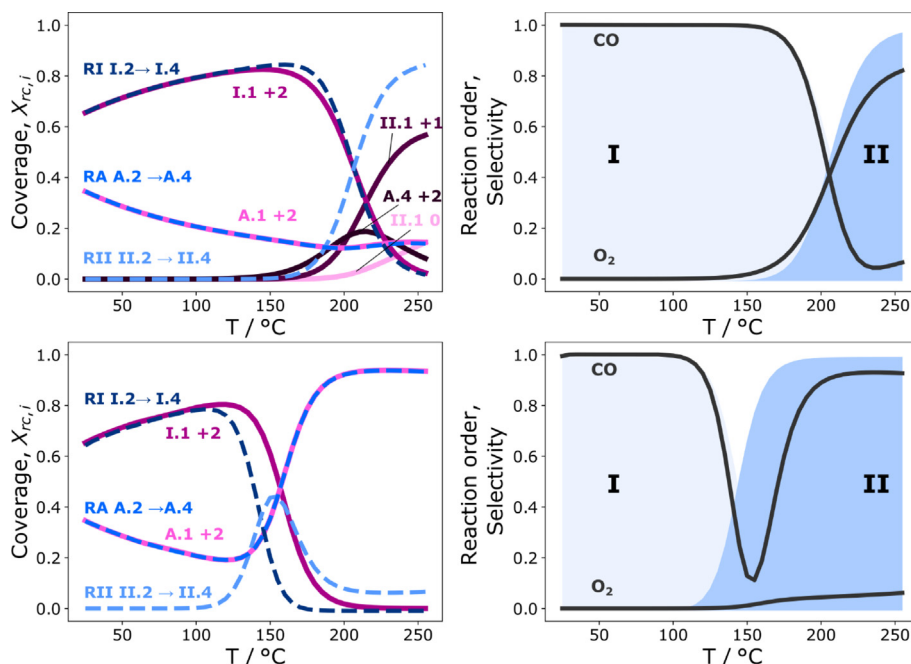

Fig. 3. Coverages of most abundant species (solid lines, see figure for assignment) and degrees of rate control (dashed lines marked RI, RII, and RA) as a function of temperature at 1 atm total pressure for 1 : 1 (top-left) and 1 : 9 (bottom-left) CO-to-O_2 ratios. Note that curves for rate control of RA and coverage of A.1 mOS 2 are directly on top of each other. Steady-state reaction orders of CO and O_2, and selectivities towards Cycle I and Cycle II as a function of temperature at 1 atm total pressure for 1 : 1 (top-right) and 1 : 9 (bottom-right) CO-to-O_2 ratios.
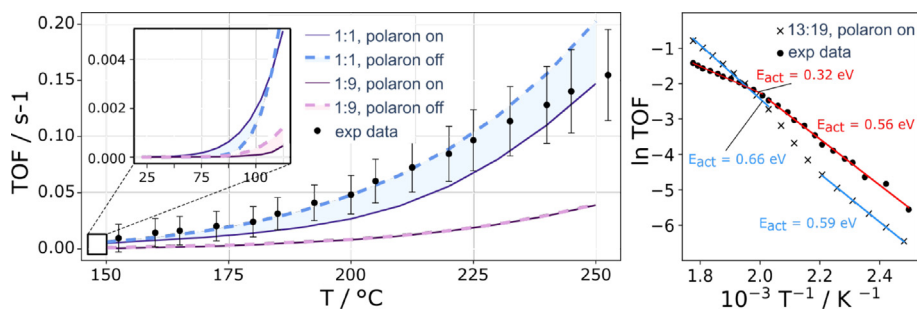
Fig. 4. Steady-state turnover frequency as a function of temperature at 1 atm total pressure for 1 : 1 (blue) and 1 : 9 (purple) CO-to-O$_2$ ratios. Full line stands for polaron hopping turned *on* and dashed line for *off*. The hybrid region where polaron hopping is only partially active has been shaded. The inset shows the low temperature regime, where the boosting behaviour of each model interchanges. The experimental reference at 13 : 19 ratio (close to 1 : 1) is denoted by black dots with error bars. The Arrhenius plots for experimental data and data from 13 : 19 gas-composition MKM are presented on the right. Note that these data are computed from CO conversion rates in Ref. [26]. For more information please see sec.tion 2.1 SI.

frequencies (TOF) obtained from the microkinetic models to previous experimental data from literature. To identify the role of the charge transfer at the interface we have tested two models, one where electron hopping is allowed and a second one were these processes are frozen. When the polaron hops are switched on, the reaction can proceed through Cycle I, which requires the SAC geometry A.4 to go from + I to + II in order to adsorb oxygen. Instead, when polaron hops are switched off, the reaction is forced to go through Cycle II, leading to lower TOF at low temperature (see insert in Fig. 4). At higher temperatures for the 1 : 1 gas-phase composition, the overall TOF is slightly lower when the polaron hops are switched on, due to the competition between Cycle I and Cycle II.

It is clear that a more oxidizing environment negatively impacts the overall performance, attaining less than a third of the 1 : 1 TOF value at 250°C, and switching the polaron hopping steps off does not lead to an appreciable change in the overall TOF for the 1 : 9 composition. This may be due to the switch-over from Cycle I to Cycle II taking place at much lower temperature as compared to the 1 : 1 case. Once Cycle II starts up, the competition between the cycles is crucial for overall TOF. There are two conditions which enable Cycle I to compete with Cycle II: (1) polarons are switched on (2) CO removal is sufficiently unfavoured. With low CO pressure, removal of the protecting CO ligand is facile, which means that Cycle II dominates regardless if polarons are switched on.

To test how well the model can reproduce the apparent activation energy, additional simulations were performed at the same 13:19 gas-phase composition as used in Ref. [26]. The apparent activation energies were determined from Arrhenius plots (Fig. 4). The experimental TOF shows a different slope above and below 225°C, resulting in two regions with different activation energies. The experimental apparent activation energy as determined from the linear fit below 225°C, is 0.56 eV. The apparent activation energy above 225°C is 0.32 eV. The Arrhenius plot for the simulated data also shows regions with different slopes, giving slightly different apparent activation energies at different temperature intervals. The change in apparent activation energy this case coincides with the selectivity switch-over from Cycle I to Cycle II. The linear fits for the simulated data were therefore done for temperature intervals where either cycle has a selectivity of over 0.8. The obtained lower temperature (Cycle I) apparent activation energy is 0.59 eV, which is in excellent agreement with the experimental value. The high temperature (Cycle II) apparent activation energy is 0.66 eV, which is higher than the experimental activation energy in this temperature region. We also tested the effect of polaron hops on the apparent activation energy, and found that when the hops are switched off, the low temperature apparent activation energy becomes 0.80 eV. The change in apparent activation energy observed when polaron hopping is not allowed is due to the reaction being forced to proceed through the more energetically demanding Cycle II. This highlights the importance of including polaron hopping steps in the reaction network, as the agreement between the experimental and modelled apparent activation energy can only be achieved if polaron hopping steps are allowed.

The presence of SAC oxidation state dynamics acts as a third reaction parameter, after the temperature and gas-phase composition. As the bulk of the oxide can be reduced the number of polarons inside of the oxide material (the 4f-band filling of the support (see Table S3)), leads to variable concentrations of Ce^{3+} ions. At large bulk reduced concentrations, entropic contributions limit the paths for the injection of electrons from the isolated metal to the support, thus suppress the dynamics of the charge transfer and maintain SA Pt in a low oxidation state.[77] From the microkinetic simulations, this could increase the yield substantially through the low-temperature regime observed in the polaron–off models. Experimentally, the bulk oxide reduction can be achieved by temperature treatments or by dopants [78].

5. Conclusions

In summary, a microkinetic model based on Density Functional Theory-computed energy profiles for CO oxidation on single Pt atoms on Ceria can be directly compared to experimental kinetics. However, to properly account for the charge transfer at the interface, the ground and low-lying potential energy surfaces need to be incorporated. Based on our model, we find that the catalytic process is characterized by two separate temperature and reactant sensitive reaction cycles (Cycle I and II). The dynamic charge transfer between the metal and the oxide enhances activity in the low temperature regime dominated by a Pt^0 active species (Cycle I). At high (over 225°C) temperatures, the mechanism switches to being less sensitive to charge transfer dynamics (Cycle II). Thus, the low-temperature oxidation rate can be improved by controlling the prevalence of the metallic state through the control of the oxygen content in the bulk of the oxide. Our results highlight the need to include the dynamic behaviour of the SAC metal oxidation states in order to produce comprehensive computational models and point towards the control of charge transfer at metal/semiconductor interfaces to improve oxidation processes.

Supporting Information Available.

All DFT calculations have been made open-access at ioChem-BD [79]: https://iochem-bd.iciq.es/browse/review-collection/100/37388/edeeb937470b10f43b7528da. The MK data is available upon a reasonable request from the authors.

Data availability

DFT data is freely shared. The link can be found from the end of the manuscript.

Declaration of Competing Interest

The authors declare that they have no known competing financial interests or personal relationships that could have appeared to influence the work reported in this paper.

Acknowledgement

Appendix A. Supplementary material

Supplementary data associated with this article can be found, in the online version, at https://doi.org/10.1016/j.jcat.2023.04.014.

References

[1] A. Wang, J. Li, T. Zhang, Heterogeneous single-atom catalysis. Nat. Rev. Chem. 2 (2018) 65–81.

[2] S. Mitchell, J. Pérez-Ramírez, Single atom catalysis: a decade of stunning progress and the promise for a bright future, Nat. Commun. 11 (2020) 4302.

[3] Q. Fu, H. Saltsburg, M. Stephanopoulos, Atomically dispersed supported metal catalysts, Science 301 (2003) 935–938.

[4] B. Qiao, A. Wang, X. Yang, L.F. Allard, Z. Jiang, Y. Cui, J. Liu, J. Li, T. Zhang, Single-atom catalysis of CO oxidation using Pt_1/FeO_x, Nat. Chem. 3 (2011) 634–641.

[5] J. Liu, Catalysis by supported single metal atoms, ACS Catal. 7 (2017) 34–59.

[6] S.K. Kaiser, Z. Chen, D. Faust Akl, S. Mitchell, J. Pérez-Ramírez, Single-atom catalysts across the periodic table, Chem. Rev. 120 (2020) 11703–11809.

[7] P. Sombut, L. Puntscher, M. Atzmueller, Z. Jakub, M. Reticcioli, M. Meier, G.S. Parkinson, C. Franchini, Role of Polarons in Single-Atom Catalysts: Case Study of Me1 [Au1, Pt1, and Rh1] on TiO_2(110). 2022; doi: 10.1007/s11244-022-01651-0, Online first article.

[8] F. Giustino, Electron-phonon interactions from first principles, Rev. Mod. Phys. 89 (2017) 015003.

[9] N. Daelman, M. Capdevila-Cortada, N. López, Dynamic charge and oxidation state of Pt/CeO_2 single-atom catalysts, Nat. Mat. 18 (2019) 1215–1221.

[10] J. Geiger, A. Sabadell-Rendón, N. Daelman, N. López, Data-driven models for ground and excited states for Single Atoms on Ceria, Npj Comput. Mater. 8 (2022) 171.

[11] H. Zhai, A.N. Alexandrova, Local fluxionality of surface-deposited cluster catalysts: the case of Pt_7 on Al_2O_3, J. Phys. Chem. Lett. 9 (2018) 1696–1702.

[12] J. Pérez-Ramírez, N. López, Strategies to break linear scaling relationships, Nature Catal. 2 (2019) 971–976.

[13] J. Jones, H. Xiong, A.T. DeLaRiva, E.J. Peterson, H. Pham, S.R. Challa, G. Qi, S. Oh, M.H. Wiebenga, X.I.P. Hernández, Y. Wang, A.K. Datye, Thermally stable single-atom platinum-on-ceria catalysts via atom trapping, Science 353 (2016) 150–154.

[14] Q. Wu, J. Ba, X. Yan, J. Bao, Z. Huang, S. Dou, D. Dai, T. Tang, W. Luo, D. Meng, Insight of Pt-support interaction in $S-Pt/Ce_{0.7}Zr_{0.3}O_2$ by in situ Raman spectroscopy, Catal. Commun. 98 (2017) 34–37.

[15] A.M. Gänzler, M. Casapu, F. Maurer, H. Störmer, D. Gerthsen, G. Ferré, P. Vernoux, B. Bornmann, R. Frahm, V. Murzin, M. Nachtegaal, M. Votsmeier, J.-D. Grunwaldt, Tuning the Pt/CeO_2 Interface by in Situ Variation of the Pt Particle Size, ACS Catal. 8 (2018) 4800–4811.

[16] X.I. Pereira-Hernández, A. DeLaRiva, V. Muravev, D. Kunwar, H. Xiong, B. Sudduth, M. Engelhard, L. Kovarik, E.J.M. Hensen, Y. Wang, A.K. Datye, Tuning $Pt-CeO_2$ interactions by high-temperature vapor-phase synthesis for improved reducibility of lattice oxygen, Nat. Commun. 10 (2019) 1358.

[17] H. Jeong, D. Shin, B.-S. Kim, J. Bae, S. Shin, C. Choe, J.W. Han, H. Lee, Controlling the oxidation state of pt single atoms for maximizing catalytic activity, Angew. Chem. Int. Edit. 59 (2020) 20691–20696.

[18] H. Jeong, O. Kwon, B.-S. Kim, J. Bae, S. Shin, H.-E. Kim, J. Kim, H. Lee, Highly durable metal ensemble catalysts with full dispersion for automotive applications beyond single-atom catalysts, Nat. Catal. 3 (2020) 368–375.

[19] A.I. Boronin, E.M. Slavinskaya, A. Figueroba, A.I. Stadnichenko, T.Y. Kardash, O.A. Stonkus, E.A. Fedorova, V.V. Muravev, V.A. Svetlichnyi, A. Bruix, K.M. Neyman, CO oxidation activity of Pt/CeO_2 catalysts below 0C: platinum loading effects, Appl. Catal. B 286 (2021) 119931.

[20] A. Beniya, S. Higashi, Towards dense single-atom catalysts for future automotive applications, Nat. Catal. 2 (2019) 590–602.

[21] L. Nie, H. Mei, H. Xiong, B. Peng, Z. Ren, X.I.P. Hernandez, A. DeLaRiva, M. Wang, M.H. Engelhard, L. Kovarik, A.K. Datye, Y. Wang, Activation of surface lattice oxygen in single-atom Pt/CeO_2 for low-temperature CO oxidation, Science 358 (2017) 1419–1423.

[22] F. Maurer, J. Jelic, J. Wang, A.M. Gänzler, P. Dolcet, C. Wöll, Y. Wang, F. Studt, M. Casapu, J.-D. Grunwaldt, Tracking the formation, fate and consequence for catalytic activity of Pt single sites on CeO_2, Nat. Catal. 10 (2020) 824–833.

[23] J. Lee, Y. Ryou, J. Kim, X. Chan, T.J. Kim, D.H. Kim, Influence of the Defect Concentration of Ceria on the Pt Dispersion and the CO Oxidation Activity of Pt/CeO_2, J. Phys. Chem. C 122 (2018) 4972–4983.

[24] M. Yoo, Y.-S. Yu, H. Ha, S. Lee, J.-S. Choi, S. Oh, E. Kang, H. Choi, H. An, K.-S. Lee, J.Y. Park, R. Celestre, M.A. Marcus, K. Nowrouzi, D. Taube, D.A. Shapiro, W. Jung, C. Kim, H.Y. Kim, A tailored oxide interface creates dense Pt single-atom catalysts with high catalytic activity, Energ. Environ. Sci 13 (2020) 1231–1239.

[25] A.M. Gänzler, M. Casapu, P. Vernoux, S. Loridant, F.J. Cadete Santos Aires, T. Epicier, B. Betz, R. Hoyer, J.-D. Grunwaldt, Tuning the structure of platinum particles on ceria in situ for enhancing the catalytic performance of exhaust gas catalysts, Angew. Chem. Int. Ed. 56 (2017) 13078–13082.

[26] D. Kunwar, S. Zhou, A. DeLaRiva, E.J. Peterson, H. Xiong, X.I. Pereira-Hernández, S.C. Purdy, R. ter Veen, H.H. Brongersma, J.T. Miller, H. Hashiguchi, L. Kovarik, S. Lin, H. Guo, Y. Wang, A.K. Datye, Stabilizing high metal loadings of thermally stable platinum single atoms on an industrial catalyst support, ACS Catal. 9 (2019) 3978–3990.

[27] S. Gatla, D. Aubert, V. Flaud, R. Grosjean, T. Lunkenbein, O. Mathon, S. Pascarelli, H. Kaper, Facile synthesis of high-surface area platinum-doped ceria for low temperature CO oxidation, Catal. Today 333 (2019) 105–112.

[28] C. Wang, X.-K. Gu, H. Yan, Y. Lin, J. Li, D. Liu, W.-X. Li, J. Lu, Water-Mediated Mars-Van Krevelen Mechanism for CO Oxidation on Ceria-Supported Single-Atom Pt 1 Catalyst, ACS Catalysis 7 (2017) 887–891.

[29] F. Dvořák, M. Farnesi Camellone, A. Tovt, N.-D. Tran, F.R. Negreiros, M. Vorokhta, T. Skála, I. Matolínová, J. Mysliveček, V. Matolín, S. Fabris, Creating single-atom Pt-ceria catalysts by surface step decoration, Nat. Commun. 7 (2016) 10801.

[30] R.H. Crabtree, H. Torrens, Encyclopedia of Inorganic Chemistry, John Wiley & Sons Ltd, Chichester, UK, 2006, pp. 1–9.

[31] X. Li, X. Yang, J. Zhang, Y. Huang, B. Liu, In Situ/Operando Techniques for Characterization of Single-Atom Catalysts, ACS Catal. 9 (2019) 2521–2531.

[32] Q. Liu, Z. Zhang, Platinum single-atom catalysts: a comparative review towards effective characterization, Catal. Sci. Tech 9 (2019) 4821–4834.

[33] D. Jiang, Y. Yao, T. Li, G. Wan, X.I. Pereira-Hernández, Y. Lu, J. Tian, K. Khivantsev, M.H. Engelhard, C. Sun, C.E. García-Vargas, A.S. Hoffman, S.R. Bare, A.K. Datye, L. Hu, Y. Wang, Tailoring the Local Environment of Platinum in Single-Atom Pt_1/CeO_2 Catalysts for Robust Low-Temperature CO Oxidation, Angew. Chem. Int. Ed. 60 (2021) 26054–26062.

[34] Y. Lu, S. Zhou, C.T. Kuo, D. Kunwar, C. Thompson, A.S. Hoffman, A. Boubnov, S. Lin, A.K. Datye, H. Guo, A.M. Karim, Unraveling the intermediate reaction complexes and critical role of support-derived oxygen atoms in CO Oxidation on Single-Atom Pt/CeO_2, ACS Catalysis 11 (2021) 8701–8715.

[35] J.K. Nørskov, F. Studt, F. Abild-Pedersen, T. Bligaard, Fundamental Concepts in Heterogeneous Catalysis, John Wiley & Sons Inc, Hoboken, New Jersey, 2014, p. 196, 1st ed.;.

[36] Q. Li, R. García-Muelas, N. López, Microkinetics of alcohol reforming for H_2 production from a FAIR density functional theory database, Nat. Commun. 9 (2018) 526.

[37] A. Bruix, J.T. Margraf, M. Andersen, K. Reuter, First-principles-based multiscale modelling of heterogeneous catalysis, Nat. Catal. 2 (2019) 659–670.

[38] M. Saeys, M.F. Reyniers, M. Neurock, G.B. Marin, Ab initio reaction path analysis of benzene hydrogenation to cyclohexane on Pt(111), J. Phys. Chem. B 109 (2005) 2064–2073.

[39] K. Alexopoulos, Y. Wang, D.G. Vlachos, First-Principles Kinetic and Spectroscopic Insights into Single-Atom Catalysis, ACS Catal. 9 (2019) 5002–5010.

[40] M. Kauppinen, M. Melander, A. Bazhenov, K. Honkala, Unraveling the Role of the $Rh - ZrO_2$ Interface in the Water-Gas-Shift Reaction via a First-Principles Microkinetic Study, ACS Catal. 8 (2018) 11633–11647.

[41] L.C. Grabow, B. Hvolbæk, H. Falsig, J.K. Nørskov, Search Directions for Direct H_2O_2 Synthesis Catalysts Starting from Au_{12} Nanoclusters, Top. Catal. 55 (2012) 336–344.

[42] K.A. Goulas, A.V. Mironenko, G.R. Jenness, T. Mazal, D.G. Vlachos, Fundamentals of C-O bond activation on metal oxide catalysts, Nat. Catal. 2 (2019) 269–276.

[43] K. Honkala, A. Hellman, I.N. Remediakis, A. Logadottir, A. Carlsson, S. Dahl, C.H. Christensen, J.K. Nørskov, Ammonia synthesis from first-principles calculations, Science 307 (2005) 555–558.

[44] A.A. Gokhale, J.A. Dumesic, M. Mavrikakis, On the mechanism of low-temperature water gas shift reaction on copper, J. Am. Chem. Soc. 130 (2008) 1402–1414.

[45] H. Wang, J.-X. Liu, L.F. Allard, S. Lee, J. Liu, H. Li, J. Wang, J. Wang, S.H. Oh, W. Li, M. Flytzani-Stephanopoulos, M. Shen, B.R. Goldsmith, M. Yang, Surpassing the

single-atom catalytic activity limit through paired Pt-O-Pt ensemble built from isolated Pt1 atoms, Nat. Commun. 10 (2019) 3808.

[46] Z. Zhang, B. Zandkarimi, A.N. Alexandrova, Ensembles of Metastable States Govern Heterogeneous Catalysis on Dynamic Interfaces, Acc. Chem. Res. 59 (2020) 16527–16535.

[47] A. Bruix, J.A. Rodriguez, P.J. Ramírez, S.D. Senanayake, J. Evans, J.B. Park, D. Stacchiola, P. Liu, J. Hrbek, F. Illas, A New Type of Strong Metal-Support Interaction and the Production of H 2 through the Transformation of Water on Pt/CeO 2 (111) and Pt/CeO x/TiO 2 (110) Catalysts, J. Am. Chem. Soc. 134 (2012) 8968–8974.

[48] J.P. Perdew, K. Burke, M. Ernzerhof, Generalized Gradient Approximation Made Simple, Phys. Rev. Lett. 77 (1996) 3865–3868.

[49] J.P. Perdew, K. Burke, M. Ernzerhof, Erratum: generalized gradient approximation made simple, Phys. Rev. Lett. 78 (1997) 1396.

[50] G. Kresse, J. Hafner, Ab initio molecular dynamics for liquid metals, Phys. Rev. B 47 (1993) 558–561.

[51] G. Kresse, J. Hafner, Ab initio molecular-dynamics simulation of the liquid-metalamorphous- semiconductor transition in germanium, Phys. Rev. B 49 (1994) 14251–14269.

[52] G. Kresse, J. Furthmiiller, Efficiency of ab-initio total energy calculations for metals and semiconductors using a plane-wave basis set, Comp. Mat. Sci. 6 (1996) 15–50.

[53] G. Kresse, J. Furthmüller, Efficient iterative schemes for ab initio total-energy calculations using a plane-wave basis set, Phys. Rev. B 54 (1996) 169.

[54] S. Fabris, G. Vicario, G. Balducci, S. De Gironcoli, S. Baroni, Electronic and atomistic structures of clean and reduced ceria surfaces, J. Phys. Chem. B 109 (2005) 22860–22867.

[55] S. Fabris, S. de Gironcoli, S. Baroni, G. Vicario, G. Balducci, Taming multiple valency with density functionals: A case study of defective ceria, Phys. Rev. B 71 (2005) 041102.

[56] N. Seriani, Z. Jin, W. Pompe, L.C. Ciacchi, Density functional theory study of platinum oxides: From infinite crystals to nanoscopic particles, Phys. Rev. B 76 (2007) 155421.

[57] R.K. Nomiyama, M.J. Piotrowski, J.L.F. Da Silva, Bulk structures of PtO and PtO2 from density functional calculations, Physical Review B 84 (2011) 100101.

[58] T. Schäfer, N. Daelman, N. López, Cerium Oxides without U: The Role of Many-Electron Correlation, J. Phys. Chem. Lett. 12 (2021) 6277–6283.

[59] G. Kresse, D. Joubert, From ultrasoft pseudopotentials to the projector augmented-wave method, Phys. Rev. B 59 (1999) 1758–1775.

[60] M. Capdevila-Cortada, M. García-Melchor, N. López, Unraveling the structure sensitivity in methanol conversion on CeO2: A DFT+U study, J. Catal. 327 (2015) 58–64.

[61] J. Neugebauer, M. Scheffler, Adsorbate-substrate and adsorbate-adsorbate interactions of Na and K adlayers on Al(111), Phys. Rev. B 46 (1992) 16067–16080.

[62] G. Makov, M.C. Payne, Periodic boundary conditions in ab initio calculations, Phys. Rev. B 51 (1995) 4014–4022.

[63] G. Henkelman, B.P. Uberuaga, H. Jónsson, A climbing image nudged elastic band method for finding saddle points and minimum energy paths, J. Chem. Phys. 113 (2000) 9901–9904.

[64] E. Pastor, J.-S. Park, L. Steier, S. Kim, M. Grätzel, J.R. Durrant, A. Walsh, A.A. Bakulin, In situ observation of picosecond polaron self-localisation in α-Fe2O3 photoelectrochemical cells, Nat. Commun. 10 (2019) 3962.

[65] J.J. Plata, A.M. Márquez, J.F. Sanz, Electron mobility via polaron hopping in bulk ceria: A first-principles study, J. Phys. Chem. C 117 (2013) 14502–14509.

[66] J.E. Sutton, A. Beste, S.H. Overbury, Origins and implications of the ordering of oxygen vacancies and localized electrons on partially reduced CeO2(111), Physical Review B - Condensed Matter and Materials Physics 92 (2015).

[67] D. Zhang, Z.-K. Han, G.E. Murgida, M.V. Ganduglia-Pirovano, Y. Gao, Oxygen-Vacancy Dynamics and Entanglement with Polaron Hopping at the Reduced CeO₂ (111) Surface, Phys. Rev. Lett. 122 (2019) 096101.

[68] A.H. Larsen, J.J. Mortensen, J. Blomqvist, I.E. Castelli, R. Christensen, M. Dulak, J. Friis, M.N. Groves, B. Hammer, C. Hargus, E.D. Hermes, P.C. Jennings, P.B. Jensen, J. Kermode, J.R. Kitchin, E.L. Kolsbjerg, J. Kubal, K. Kaasbjerg, S. Lysgaard, J.B. Maronsson, T. Maxson, T. Olsen, L. Pastewka, A. Peterson, C. Rostgaard, J. Schiøtz, O. Schütt, M. Strange, K.S. Thygesen, T. Vegge, L. Vilhelmsen, M. Walter, Z. Zeng, K.W. Jacobsen, The Atomic Simulation Environment—a Python Library for Working with Atoms, J. Phys. Condens. Mat. 29 (2017) 273002.

[69] S.R. Bahn, K.W. Jacobsen, An Object-Oriented Scripting Interface to a Legacy Electronic Structure Code, Comput. Sci. Eng. 4 (2002) 56–66.

[70] D.J. Dooling, L.J. Broadbelt, Generic Monte Carlo Tool for Kinetic Modeling, Ind. Eng. Chem. Res. 40 (2001) 522–529.

[71] P. Virtanen, R. Gommers, T.E. Oliphant, M. Haberland, T. Reddy, D. Cournapeau, E. Burovski, P. Peterson, W. Weckesser, J. Bright, S.J. van der Walt, M. Brett, J. Wilson, K.J. Millman, N. Mayorov, A.R.J. Nelson, E. Jones, R. Kern, E. Larson, C.J. Carey, İ. Polat, Y. Feng, E.W. Moore, J. VanderPlas, D. Laxalde, J. Perktold, R. Cimrman, I. Henriksen, E.A. Quintero, C.R. Harris, A.M. Archibald, A.H. Ribeiro, F. Pedregosa, P. van Mulbregt, SciPy 1.0 Contributors, SciPy 1.0: Fundamental Algorithms for Scientific Computing in Python, Nat. Methods 17 (2020) 261–272.

[72] M. Huang, S. Fabris, Role of surface peroxo and superoxo species in the low-temperature oxygen buffering of ceria: Density functional theory calculations, Phys. Rev. B 75 (2007) 081404.

[73] W. Wan, J. Geiger, N. Berdunov, M. Lopez Luna, S.W. Chee, N. Daelman, N. López, S. Shaikhutdinov, B. Roldan Cuenya, Highly stable and reactive platinum single atoms on oxygen plasma-functionalized CeO₂ surfaces: nanostructuring and peroxo effects, Angew. Chem. Int. Ed. 61 (2022) e202112640.

[74] J. Xu, D. Mullins, S.H. Overbury, CO desorption and oxidation on CeO2-supported Rh: Evidence for two types of Rh sites, J. Catal. 243 (2006) 158–164.

[75] M. Capdevila-Cortada, N. López, Entropic contributions enhance polarity compensation for CeO2(100) surfaces, Nat. Mater. 16 (2017) 328–334.

[76] M. Bugnet, S.H. Overbury, Z.L. Wu, T. Epicier, Direct visualization and control of atomic mobility at 100 surfaces of ceria in the environmental transmission electron microscope, Nano Lett. 17 (2017) 7652–7658.

[77] J. Geiger, N. López, Coupling metal and support redox terms in single-atom catalysts, J. Phys. Chem. C 126 (2022) 13698–13704.

[78] J.-F. Jerratsch, X. Shao, N. Nilius, H.-J. Freund, C. Popa, M.V. Ganduglia-Pirovano, A.M. Burow, J. Sauer, Electron localization in defective ceria films: a study with scanning-tunneling microscopy and density-functional theory, Phys. Rev. Lett. 106 (2011) 246801.

[79] M. Álvarez-Moreno, C. de Graaf, N. López, F. Maseras, J.M. Poblet, C. Bo, Managing the computational chemistry big data problem: The ioChem-BD Platform, J. Chem. Inf. Model. 55 (2015) 95–103.